Direct Numerical Simulation of Vortex Breakdown in Evaporating Dilute Sprays

Jacopo Liberatori[1] · Francesco Battista[1] · Federico Dalla Barba[2] · Pietro Paolo Ciottoli[1]

Abstract

The effects of different vortex breakdown states on the evaporation process characterizing air-acetone vapor swirling jets laden with liquid acetone droplets in the dilute regime are discussed based on results provided by direct numerical simulations. Adopting the point-droplet approximation, the carrier phase is solved using an Eulerian framework, whereas a Lagrangian tracking of the dispersed phase is used. Three test cases are investigated: one with fully-turbulent pipe inflow conditions and two with a laminar Maxworthy velocity profile at different swirl rates. Consequently, turbulent, bubble-type, and regular conical vortex breakdown states are established. Following phenomenological and statistical analyses of both phases, a significant enhancement of the overall droplet evaporation process due to the onset of the conical vortex breakdown is observed due to the strongest centrifugal forces driving the entire liquid drops towards the low-saturation mixing layer of the jet. The effects of droplet inertia on evaporation are isolated through an additional set of simulations where liquid droplets are treated as Lagrangian tracers. While it is found that inertial effects contribute to enhanced vaporization near the mixing layer under bubble vortex breakdown conditions, droplet inertia plays a secondary role under both turbulent and conical vortex breakdown due to intense turbulent mixing and high centrifugal forces, respectively.

1 Introduction

Droplet-laden swirling jets appear in various technological processes, particularly in combustion devices. In this regard, internal combustion engines (ICEs), gas turbine combustors (GTCs), and liquid rocket engines (LREs) make use of swirled inflows for either or both of the oxidizer and fuel sides. Although the swirling motion may be imposed through different means, the common objective is to enhance fuel-oxidizer mixing and promote aerodynamic flame stabilization (Syred and Beér 1974; Lilley 1977). Nonetheless, swirling flames typically show a less prominent extent compared with their non-swirled counterparts

---

Francesco Battista, Federico Dalla Barba and Pietro Paolo Ciottoli contributed equally to this work.

Extended author information available on the last page of the article

(Menon and Ranjan 2016), and this compactness helps prevent the flame from impinging on the combustion chamber walls, thus reducing the thermal loads the whole combustion system may suffer.

On the one hand, optimal fuel-oxidizer mixing is typically achieved by injecting liquid fuel into the swirling oxidizer stream to facilitate liquid breakup, dispersion, and consequent vaporization. For example, in the effort to achieve ultra-low NOx aviation gas turbines, lean direct injection (LDI) combustors exploit such a strategy to form extremely lean mixtures with an exceptional degree of premixedness (Luo et al. 2011). On the other hand, flame stabilization is a direct consequence of the flow patterns which arise from moderately to highly swirling flows. In this regard, it is well-known how exceeding a critical swirl degree results in the onset of the vortex breakdown (VB) phenomenology (Billant et al. 1998; Lucca-Negro and O'Doherty 2001), namely, the bubble-type and the regular conical breakdown states. Swirling jets undergoing VB show extensive reverse flow regions, which are responsible for recirculating hot-gas combustion products and thus serve as aerodynamic flame holders and enhance the level of mixing and fuel entrainment in the proximity of the liquid injector's nozzle exit. Notably, the onset of a VB-induced recirculation zone is a widely employed strategy to enhance flame stability in stationary gas turbines and aeroengines (Wu et al. 2016; Shen et al. 2020). At the same time, the flame typically resides in the shear layer originating in the near-field region.

The numerical modeling of spray swirling jets is not a trivial task due to both the peculiar features of the flow field and the impact of swirling motion on the several breakup processes which lead to droplet formation in a combustion device (Faeth et al. 1995). In this sense, following the evolution of a liquid jet discharging from an injector nozzle, it is possible to identify different regimes (Apte and Moin 2011): (i) *primary breakup zone*, characterized by the disintegration of the liquid sheet into ligaments; (ii) *dense spray regime*, showing relevant liquid coalescence phenomena; (iii) *secondary breakup zone*, where large drops are formed, and the volume fraction of the liquid phase significantly decreases; (iv) *dilute regime*, where liquid vaporization and fuel-oxidizer mixing take place.

A numerical model able to capture the entirety of features evidencing in the processes mentioned above should handle a continuum formulation in the *primary breakup zone*, account for droplet collision, coalescence, and deformation in the *dense spray regime*, and reproduce the phenomena taking place in the *dilute regime*, which are typically characterized by extremely different length and time scales. Nonetheless, in practice, the distinction between these regimes is not straightforward.

Given these considerations, numerical approaches dealing with the modeling of multiphase flows typically resort to Eulerian-Eulerian, Eulerian–Lagrangian, and statistical methods. The Eulerian-Eulerian approach provides the opportunity to employ consistent numerical methods for both the carrier and the disperse phases, in which both are solved using an Eulerian framework (Druzhinin and Elghobashi 1998; Balachandar and Eaton 2010). Drawbacks of this methodology consist in the degree of modeling required by the transport equations for the liquid phase and numerical instability issues which may arise in the presence of significant concentration gradients (Menon and Ranjan 2016). Conversely, the Eulerian–Lagrangian approach hinges on the point-droplet approximation and the Lagrangian tracking of the dispersed phase (Elghobashi 1991; Casciola et al. 2010). An Eulerian–Lagrangian approach is hence adopted in the present work, being the most commonly employed methodology when dealing with multiphase flow systems due to its ability to handle a variety of processes, i.e., polydispersity, droplet-droplet and droplet-wall interaction, and droplet breakup. However, the computational burden associated with this approach may increase if a large number of liquid droplets is required to reconstruct

accurately the Eulerian field of the vaporized liquid's mass fraction. In this regard, a reduction of the computational cost can be attained by tracking *parcels*, i.e., ensembles of liquid droplets which share the same properties, instead of individual droplets (Subramaniam 2013). Nonetheless, hybrid approaches which resort to an Eulerian-Eulerian fashion to model the dense regime that originates in the proximity of the injector and to an Eulerian–Lagrangian fashion to capture the complete breakup process downstream, have been proposed, see e.g. Arienti et al. (2013) for the modeling of like-on-like jet impingement of relevance to liquid rocket engine combustion. An alternative solution is represented by the fully Lagrangian approach (FLA) (Osiptsov 2000), which incorporates the assumption of droplet phase continuity into the Eulerian–Lagrangian framework. Notably, a generalized FLA was recently employed to address polydisperse two-phase flows (Li and Rybdylova 2021). Lastly, within statistical approaches, the spray is modeled via a droplet distribution function (DDF) (Pai and Subramaniam 2006), which accounts for the droplet density in position-velocity-radius space and is governed by an ad-hoc transport equation, known as the Williams' spray equation (Williams 1958). However, due to the necessity of a high-order numerical treatment, statistical methods are computationally expensive and typically limited to studying prototypical configurations (Menon and Ranjan 2016).

Several numerical studies on spray swirling jets under non-reactive and reactive conditions in realistic and lab-scale swirl combustors, accompanied by vast experimental databases, can be found in the literature (Sankaran and Menon 2002; Patel and Menon 2008; Senoner et al. 2009; Apte and Moin 2011; Luo et al. 2011; Jones et al. 2014; Puggelli et al. 2016; Giusti et al. 2016; Wu et al. 2016; Eckel et al. 2019; Shen et al. 2020; Ciottoli et al. 2021). In these studies, major observables of interest are the size of the VB-induced recirculation zone and how it is affected by heat release, the fuel vapor distribution and mixing efficiency, the preferential location of different burning modes, and the spatial distribution of droplets' Sauter mean diameter. However, only a small subset of these works focus on how flow patterns associated with the carrier swirling motion impact droplet dynamics, namely, spray dispersion and vaporization. In Jones et al. (2014), the authors investigated fuel spray processes occurring in the DLR Generic Single Sector Combustor (Meier et al. 2012), where liquid kerosene is injected into swirling air, carrying out two large eddy simulations (LES) dealing with both reacting and non-reacting operating conditions. While the authors adopted a Lagrangian formulation of the dispersed phase, the effects of sub-grid scale fluctuations on droplet dispersion and evaporation were accounted for through stochastic models. Small droplets were observed to undergo dispersion more rapidly, thus populating mostly the outer zone of the spray cone. On the other hand, larger droplets were predominantly present in the central zone due to their higher inertia, eventually leading to a complex flame structure in that premixed and non-premixed combustion modes may coexist due to the variety of evaporation time scales. In Sankaran and Menon (2002), the authors investigated the unsteady interactions between spray dispersion, vaporization, heat release, and swirling intensity manifesting in a dual annular counter-rotating swirling (DACRS) gas turbine combustor through two different sets of LES in an Eulerian–Lagrangian fashion. In particular, two swirling levels were considered under both reacting and non-reacting conditions, the higher one resulting in the onset of a bubble-type VB. On the one hand, in the absence of VB phenomenology, spray dispersion in the near field is highly modulated by the highly-coherent vortex structures found in the shear layer. Conversely, dispersion becomes significant as the onset of three-dimensional instabilities progressively destroys these structures. On the other hand, the increase in swirl intensity leads to a faster decay in the degree of coherence of vortex structures, resulting in enhanced spray dispersion. However, a significant presence of liquid droplets can still be observed within

the VB-associated recirculation region. In Senoner et al. (2009), the authors investigated through LES the liquid-phase dynamics in a swirl-stabilized laboratory burner, known as the MERCATO burner, fueled with liquid Jet-A kerosene. Given that the swirling degree imparted to the incoming air resulted in the onset of a conical VB, droplet preferential concentration was observed: low droplet density was registered inside the VB-associated reverse flow zone. In contrast, dense pockets of droplets were found in the shear layer originating in the proximity of the injector exit section. In Gui et al. (2011), the authors carried out several direct numerical simulations (DNS) to investigate spray dispersion in a droplet-laden swirling jet, showing the onset of a bubble-type VB. In particular, different simulations were carried out, denoting the impact of droplet Stokes number and mass loading on preferential concentration phenomena. In this regard, the authors highlighted that small droplets, characterized by a low Stokes number, were predominantly dispersed to the peripheral zone of the domain by the large-scale vortical structures enclosing the bubble VB. On the other hand, larger droplets, providing completely different dynamical response properties, were observed to be dispersed almost axisymmetrically around the periphery of the VB-induced recirculation region. In contrast, the dispersion of even larger droplets barely exhibited a dependence on large-scale vortex structures, and no radial dispersion was observed. Nonetheless, heavy mass loading was considered responsible for decreased gas-liquid momentum exchange, resulting in less effective inter-phase energy transportation for the dispersion of individual droplets. In a previous work by our research group (Ciottoli et al. 2021), a set of DNS were conducted to assess the effects of swirled inflows on the evaporation of dilute acetone droplets dispersed in turbulent jets discharging into an open environment, already investigated in Dalla Barba and Picano (2018) in the absence of swirl. In particular, swirl was imposed at the jet inflow section by means of fully turbulent velocity profiles resulting from a companion DNS of a turbulent rotating pipe flow. Adopting an Eulerian–Lagrangian approach, an enhancement of the droplet vaporization rate with increasing swirl velocities was observed, although no VB phenomenology arose. In particular, this augmented evaporation was ascribed to the enhanced dry air entrainment and to the swirl-induced centrifugal forces acting on liquid droplets in the jet shear layer close to the injection orifice.

Nonetheless, further insight is needed into how the flow field originating from VB phenomenology in swirling jets affects droplet dispersion and vaporization. In this regard, the present work aims at assessing, via DNS, the liquid-phase dynamics induced by different VB states, namely, the bubble-type VB and the regular conical VB, under both laminar and fully turbulent inflow conditions.

Lastly, the present work is framed in a larger research project aimed at the numerical modeling of multiphase reacting flows in aeronautical and liquid rocket propulsion via Reynolds-averaged Navier-Stokes (RANS) and LES approaches (Battista et al. 2015; Ciottoli et al. 2020). In fact, as evidenced in our previous work (Liberatori et al. 2023), the insights into the spray structure and gas-liquid interaction provided by DNS serve as a high-fidelity benchmark. With respect to the latter, Bayesian calibration techniques (MacKay 2005) can be employed to statistically characterize the uncertainty sources which affect the sub-models embedded into the lower-fidelity approaches, i.e., LES and RANS, addressing liquid phase behavior in multiphase reacting flows, e.g., droplet dispersion. In this regard, the impact of spray sub-models' uncertain parameters on the major observables can be assessed through non-intrusive spectral projection techniques (Ciottoli et al. 2020b; Liberatori et al. 2021; Cavalieri et al. 2023; Liberatori et al. 2023), thus returning an overview of those model uncertainties that require further investigation through high-fidelity campaigns.

2 Theoretical and Numerical Formulation

The numerical analysis carried out in the present work hinges on the DNS solution of evaporating sprays discharging in an open environment, resorting to an Eulerian–Lagrangian methodology. A detailed description of the computational framework can be found in our previous research studies (Dalla Barba and Picano 2018; Ciottoli et al. 2021). Nonetheless, the key aspects are shortly recalled in the following for the sake of the self-consistency of the document.

A low-Mach number asymptotic formulation of the Navier–Stokes equations is adopted to describe the Eulerian gaseous phase (Majda and Sethian 1985), while a point-droplet approximation is adopted to simulate the behavior of liquid droplets. The coupling between the carrier phase and the dispersed phase is reproduced employing three sink-source terms in the right-hand side of the mass, momentum, and energy equations (Miller and Bellan 1999; Bukhvostova et al. 2014; Mashayek 1998). Consistently with the dilute spray regime, droplet collision, and coalescence phenomena are discarded.

The full set of Navier–Stokes equations employed follows:

$$\frac{\partial \rho}{\partial t} + \nabla \cdot (\rho \boldsymbol{u}) = S_m, \tag{1}$$

$$\frac{\partial}{\partial t}\left(\rho Y_v\right) + \nabla \cdot \left(\rho Y_v \boldsymbol{u}\right) = \nabla \cdot \left(\rho \mathcal{D} \nabla Y_v\right) + S_m, \tag{2}$$

$$\frac{\partial}{\partial t}(\rho \boldsymbol{u}) + \nabla \cdot (\rho \boldsymbol{u} \otimes \boldsymbol{u}) = \nabla \cdot \boldsymbol{\tau} - \nabla P + \boldsymbol{S}_p, \tag{3}$$

$$\nabla \cdot \boldsymbol{u} = \frac{\gamma - 1}{\gamma} \frac{1}{p_0} \left[\nabla \cdot (k \nabla T) + S_e - L_v^0 S_m \right], \tag{4}$$

$$p_0 = \rho R_m T, \tag{5}$$

where $\boldsymbol{u}$, ρ, and T are the velocity, density, and temperature of the carrier mixture, respectively, while $Y_v = \rho_v/\rho$ is the vapor mass fraction field, ρ_v being the vapor partial density. The viscous stress tensor is $\boldsymbol{\tau} = \mu\left(\nabla \boldsymbol{u} + \nabla \boldsymbol{u}^T\right) - (2/3)\mu(\nabla \cdot \boldsymbol{u})\boldsymbol{I}$, with μ the dynamic viscosity of the carrier mixture. Assuming calorically perfect chemical species and a reference temperature $T_0 = 0$ K, we denote L_v^0 as the latent heat of vaporization of the liquid phase evaluated at the reference temperature T_0. The thermodynamic and hydrodynamic pressure fields are denoted as p_0 and P, respectively, where the former is uniform over the computational domain and constant over time due to the free convection boundary conditions adopted in the present study. The thermal conductivity and the specific heat ratio of the carrier mixture are k and γ, respectively, whereas the binary mass diffusion coefficient of the vapor is denoted as $\mathcal{D}$. The carrier phase is assumed to be governed by the ideal gas law (5), where $R_m = \bar{R}/W_m$ is the specific gas constant of the mixture, W_m is its molar mass and $\bar{R}$ is the universal gas constant.

In the right-hand sides of the mass, momentum, and energy equations, S_m, $\boldsymbol{S}_p$, and S_e denote the sink-source terms which account for the forcing of the dispersed phase on the carrier one. These latter are provided below in discrete notation:

$$S_m = -\sum_{i=1} \frac{dm_{D,i}}{dt} \delta(\boldsymbol{x} - \boldsymbol{x}_{D,i}), \tag{6}$$

$$\boldsymbol{S}_p = -\sum_{i=1} \frac{d}{dt}(m_{D,i}\boldsymbol{u}_{D,i})\delta(\boldsymbol{x} - \boldsymbol{x}_{D,i}), \tag{7}$$

$$S_e = -\sum_{i=1} \frac{d}{dt}(m_{D,i}c_l T_{D,i})\delta(\boldsymbol{x} - \boldsymbol{x}_{D,i}), \tag{8}$$

where the Lagrangian variables $\boldsymbol{x}_{D,i}$, $\boldsymbol{u}_{D,i}$, $m_{D,i}$, and $T_{D,i}$ represent the position, velocity, mass, and temperature of the ith droplet, respectively, while c_l is the specific heat of the liquid phase. The discrete delta function, $\delta(\boldsymbol{x} - \boldsymbol{x}_{D,i})$, accounts for the fact that each sink-source term acts only at the domain locations occupied by each point-droplet. In this frame, the kinematics, dynamics, and thermodynamics of the dispersed phase are completely described by the Lagrangian equations reported in Ciottoli et al. (2021).

2.1 Numerical Schemes

The Eulerian Equations (1) and (5) are discretized on a cylindrical staggered mesh through second-order, central finite differences schemes. The equations are integrated in time adopting a low-storage, third-order, Runge–Kutta scheme (Battista et al. 2014; Rocco et al. 2015; Dalla Barba and Picano 2018). To avoid unphysical oscillations for the mass fraction, Y, in Equation (2), the convective term of the scalar quantities is discretized using a bounded central difference scheme designed to avoid spurious oscillation, as detailed in Waterson and Deconinck (2007). Moreover, in the limit of dilute systems, the variations of volume fraction in the dynamical Eulerian equations are neglected as in Mashayek (1998); Miller and Bellan (1999).

Lastly, the droplet mass, momentum, and temperature laws are evolved through a Lagrangian approach. The temporal integration uses the same Runge–Kutta scheme adopted by the Eulerian algorithm. The Eulerian quantities at the droplet positions are computed using a second-order accurate polynomial interpolation.

3 Computational Setup

All the presented DNS computations reproduce an air-acetone vapor jet laden with liquid acetone droplets in the dilute regime, consistently with what was already investigated in Dalla Barba and Picano (2018); Ciottoli et al. (2021). In this regard, it is worth recalling that the flow conditions at the inlet section of the non-swirled jet flow studied in Dalla Barba and Picano (2018); Ciottoli et al. (2021), from now on referred to as the non-swirled baseline case, are comparable to those adopted in the well-controlled experiments on dilute coaxial sprays published by the group of Chen et al. (2006) and Villermaux et al. (2017), except for a lower Reynolds number. The experiments use acetone droplets dispersed in the air at the temperature of 275.15 K in non-reactive and reactive conditions.

In the present numerical study, the gas–vapor mixture is injected into an open environment through an orifice of radius $R = 5 \cdot 10^{-3}$ m at a bulk axial velocity $U_{z,0} = 8.1$ m/s. The distribution of droplets on the inflow section consists of a random position of

monodisperse, liquid-acetone droplets with an initial radius $r_{D,0} = 6$ μm, which locally take the velocity of the carrier phase. The ambient pressure is set to $p_0 = 101300$ Pa; the injection temperature is fixed to $T_0 = 275.15$ K for both the carrier and the dispersed phases. The injection flow rate of the gaseous phase is kept constant, fixing a bulk Reynolds number Re $= 2U_{z,0}R/\nu = 6000$, $\nu = 1.35 \cdot 10^{-5}$ m^2/s being the kinematic viscosity. A nearly-saturated condition is prescribed for the air-acetone vapor mixture at the inflow section, $S = Y_v/Y_{v,s} = 0.99$, where S is the saturation, Y_v is the actual vapor mass fraction on the inflow section and $Y_{v,s}(p_0, T_0)$ is the vapor mass fraction in a fully-saturated condition evaluated at the inflow temperature and pressure. The acetone-to-air mass flow rate ratio is set to $\Psi = \dot{m}_{act}/\dot{m}_{air} = 0.28$, $\dot{m}_{act} = \dot{m}_{act,l} + \dot{m}_{act,v}$ being the sum of the liquid, $\dot{m}_{act,l}$, and gaseous, $\dot{m}_{act,v}$, acetone mass flow rates. This configuration corresponds to a bulk volume fraction of the liquid phase $\Phi = 8 \cdot 10^{-5}$. The thermodynamic and physical properties of the vapor gas and liquid phases are summarized in Table 1.

Three direct numerical simulations of air-acetone vapor swirling jets laden with liquid acetone droplets are presented in this study, dealing with different inflow velocity conditions: (i) one simulation with fully turbulent-pipe inflow velocity conditions; (ii) two simulations with inflow velocity conditions dictated by the laminar Maxworthy profile, at two different swirl levels. In this regard, from now on, the swirl level resulting from inflow velocity conditions will be measured through an integral swirl number, $S_{\theta z}$. Following the analysis provided in Örlü and Alfredsson (2008), the latter is defined as the ratio of the azimuthal momentum, G_θ, to the axial momentum, G_z, multiplied by the jet orifice radius, R:

Table 1 Thermodynamic and physical properties of acetone and dry air employed in the numerical simulations

p_0 [Pa]	101,300	W_g [kg/mol]	$2.90 \cdot 10^{-2}$
T_0 [K]	275.15	W_l [kg/mol]	$2.90 \cdot 10^{-2}$
$U_{z,0}$ [m/s]	8.10	k_g [W/(m K)]	$2.43 \cdot 10^{-2}$
μ [kg/(m s)]	$1.75 \cdot 10^{-5}$	k_l [W/(m K)]	$1.83 \cdot 10^{-1}$
$c_{p,g}$ [J/(kg K)]	1038	$\mathcal{D}$ [m^2/s]	$1.10 \cdot 10^{-5}$
$c_{p,v}$ [J/(kg K)]	1300	ρ_l [kg/m^3]	800
c_l [J/(kg K)]	2150	L_v [J/kg]	530,000
R [m]	$5 \cdot 10^{-3}$	Ψ [–]	0.28
Φ [–]	$8 \cdot 10^{-5}$	ν [m^2/s]	$1.35 \cdot 10^{-5}$
$r_{D,0}$ [m]	$6 \cdot 10^{-6}$	Re $= 2U_{z,0}R/\nu$ [–]	6000

The pressure p_0 is constant over time and space due to the low-Mach number formulation and open environmental conditions. The temperature, T_0, the bulk velocity, $U_{z,0}$, and the dynamic and kinematic viscosity, μ and ν, are evaluated at the inflow section. The constant-pressure specific heat capacity of the gas and vapor are $c_{p,g}$ and $c_{p,v}$, respectively, while the liquid specific heat capacity is c_l. The molar masses and the thermal conductivities of the gas and the liquid are W_g, W_l, k_g, and k_l, respectively. $\mathcal{D}$ is the mass binary diffusion coefficient of the vapor into the gas. L_v and ρ_l are the latent heat of vaporization and the liquid density evaluated at the inflow temperature, respectively. The Reynolds number, the orifice radius, and the droplets' initial radius are Re, R, and $r_{D,0}$, respectively. In contrast, $\Psi = \dot{m}_{act}/\dot{m}_{air}$ and Φ are the acetone-to-air mass flow rate ratio and the bulk volume fraction of the liquid phase, respectively

$$S_{\theta z} = \frac{G_\theta}{RG_z} = \frac{\int_0^\infty r^2 \left(U_z U_\theta + \overline{u_z u_\theta} \right) dr}{R \int_0^\infty r \left[U_z^2 - \frac{U_\theta^2}{2} + \overline{u_z^2} - \frac{\overline{u_\theta^2} + \overline{u_r^2}}{2} \right] dr}, \tag{9}$$

where z, θ, and r denote the axial, azimuthal, and radial directions, respectively. In this frame, upper-case letters denote mean velocity components, lower-case letters indicate fluctuating velocity components, and the overbar denotes time averaging. Therefore, Equation (9) provides a measure of the swirl level, accounting for mean axial and azimuthal velocity components and turbulent stresses. Lastly, to calculate the integral swirl number, $S_{\theta z}$, the radial distributions of the quantities appearing in Equation (9) are taken just downstream of the jet orifice, namely, at $z/R = 0.25$.

The following sections report a detailed description of the test case configurations investigated in the present study.

3.1 Laminar Maxworthy Inflow

For what concerns the set of two laminar-inflow simulations, the swirling motion is imparted to the fluid by imposing a Maxworthy velocity profile (Ruith et al. 2004) at the jet inflow section, i.e., on the base of the cylindrical domain. The latter velocity profile, which is intended to model the high entrainment occurring in swirling jets discharging into open environments, is typically provided in a dimensionless form. In particular, velocity components are scaled by the centerline axial velocity, while the dimensionless radial distance from the jet axis, r, is defined as the ratio of the dimensional distance from the jet axis to the core radius, R. Thus, the dimensionless azimuthal, radial, and axial velocity components read:

$$\begin{cases} U_\theta(r) = \frac{Sr}{2} \left[1 - \mathrm{erf}\left(\frac{r-1}{\delta_{SL}} \right) \right], \\ U_r(r) = 0, \\ U_z(r) = 1 - \frac{\alpha-1}{2\alpha} \left[1 + \mathrm{erf}\left(\frac{r-1}{\delta_{SL}} \right) \right], \end{cases} \tag{10}$$

where S represents the swirl rate, α denotes the core-to-coflow axial velocity ratio, expressing the ratio of the centerline axial velocity to the freestream velocity, and δ_{SL} indicates the dimensionless shear layer thickness of the swirling jet.

While the latter is fixed at $\delta_{SL} = 0.2$, no coflow is imposed at the jet inflow section for either laminar-inflow simulation, i.e., $\alpha = \infty$. Thus, the axial velocity component reads:

$$U_z(r) = 1 - \frac{1}{2} \left[1 + \mathrm{erf}\left(\frac{r-1}{\delta_{SL}} \right) \right]. \tag{11}$$

Furthermore, within the set of laminar-inflow simulations, two swirl levels are investigated, i.e., $S = 1.4$ and $S = 2.0$, naming the MPI-S140 and MPI-S200 test cases, respectively, where MPI stands for *Maxworthy-profile inflow*. In contrast, the injection flow rate of the gaseous phase is kept constant; namely, the bulk axial velocity is fixed at $U_{z,0} = 8.1$ m/s.

The jet computational domain consists of a cylinder extending for $2\pi \times 56R \times 90R$ in the azimuthal, θ, radial, r, and axial, z, directions. In this regard, the significant size of the domain ensures the development of the swirling jets is not affected by boundary

conditions, even in the case of a conical VB regime, which is characterized by a prominent jet spreading in the radial direction and a vast recirculation region that extends axially. The domain is discretized using $N_\theta \times N_r \times N_z = 128 \times 375 \times 737$ nodes distributed on a staggered mesh. The flow is injected at the center of one base of the cylindrical domain and streams out towards the other base. A fixed velocity condition is imposed on the pipe walls. A convective condition is adopted at the outlet. In contrast, an adiabatic traction-free condition is prescribed on the side surface of the cylindrical domain to mimic an open environment and make the entrainment of external fluid possible. In conclusion, Fig. 1 shows a portion of the cylindrical domain for the MPI-S140 and MPI-S200 test cases. In particular, it was decided to realize a close-up of the domain to clearly highlight the jet topology, i.e., the jet spreading and the establishment of the VB-induced reverse flow zone, which would otherwise result pretty difficult by providing an overview of the complete computational domain. For this reason, a cropped view of the computational domain is often employed to illustrate results in the remainder of the text.
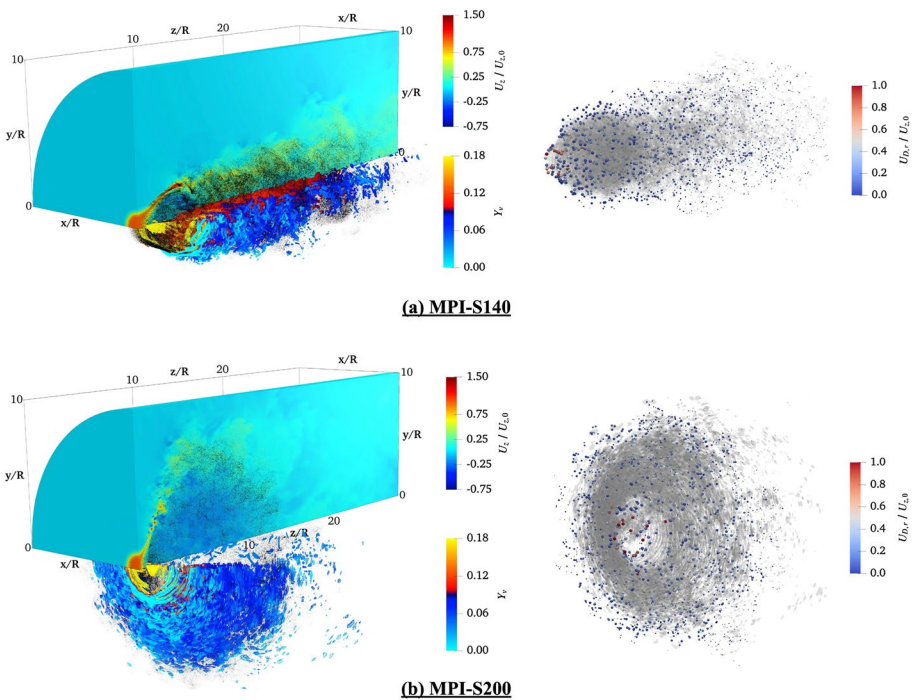
(a) MPI-S140

(b) MPI-S200

Fig. 1 Laminar inflow test cases: **a** MPI-S140, **b** MPI-S200. On the left: a sketch of a portion of the 3D cylindrical domain is illustrated; on the top, the colors contour the axial instantaneous velocity field within the jet, normalized by the bulk axial velocity, $U_{z,0}$; on the bottom, coherent vortex structures are visualized through Q-criterion isosurfaces, $Q = 0.1$, colored by the vapor mass fraction field; the whole droplet population is plotted with uniform-radius black points, i.e., droplets are not scaled by their size. On the right, in correspondence of the same time step: Q-criterion isosurfaces, $Q = 0.1$, are reported in grey; liquid droplets are scaled by their radius and colored by their radial velocity, $U_{D,r}$, normalized by $U_{z,0}$. Note that a different point of view was adopted to provide a clear insight into droplet spatial distribution, which could result in seeming inconsistency between the two figures

3.2 Turbulent-Pipe Inflow

In the turbulent-pipe simulation, from now on denoted as TPI-Sw250, where TPI stands for *turbulent-pipe inflow*, the inflow velocity conditions are obtained by assigning a fully turbulent velocity at the jet inflow section via a Dirichlet condition. A companion three-dimensional DNS reproducing a fully developed, turbulent pipe flow generates the two-dimensional inflow velocity field. In this regard, the prescribed inflow condition is extracted from a cross-sectional slice of the pipe. The flow is injected through a center orifice in the lower domain base, the remaining part impermeable and adiabatic. The simulation is characterized by a bulk swirl number $Sw = U_{\theta,max}/U_{z,0} = 2.5$, where $U_{\theta,max}$ is the maximum value taken by the azimuthal velocity along the inflow cross-section of the cylindrical domain. In contrast, the velocity $U_{z,0}$ is the mean, bulk axial velocity computed from the pipe axial flow rate, i.e., $U_{z,0} = \frac{1}{R}\int_0^R \langle u_z \rangle (r) dr$. The integrand is the mean axial velocity in the pipe averaged concurrently over time and along the z and θ directions. Consistently with (Dalla Barba and Picano 2018; Ciottoli et al. 2021), the rotating turbulent pipe technique was chosen following the experimental studies reported in Facciolo et al. (2007), which demonstrated its effectiveness in studying swirling flows of practical interest. In particular, a periodic pipe flow simulation, in which the axial flow is driven by a pressure gradient and the pipe wall is rotating about the axis, is employed to generate the inflow boundary conditions extends for $2\pi \times 1R \times 8R$ in the azimuthal, θ, radial, r, and axial, z, directions, and is discretized with a staggered mesh containing $N_\theta \times N_r \times N_z = 128 \times 80 \times 128$ nodes to match the corresponding jet computational grid at the pipe discharge. In this regard, the cylindrical domain remains unaltered compared with the Maxworthy inflow configurations. In particular, no difference can be envisaged regarding domain discretization and boundary conditions, except for the imposition of a uniform 10% axial coflow over the first 8 radii of the jet inflow section, i.e., $U_{z,cof} = 0.1 U_{z,0}$ on the base of the cylindrical domain. This is to avoid the establishment of Coanda effect, i.e., the tendency of a fluid jet to follow the curvature of a solid surface. Specifically, in the absence of coflow or even under negligible coflow velocity, the inflow plane could be approximated as a solid wall. In this sense, the Coanda effect may arise, which would cause the flow sheet issuing into the cylindrical domain to be attracted towards the inflow plane (Moise and Mathew 2021), leading to a completely different jet topology. In Fig. 2, is shown a snapshot of the cylindrical domain for the TPI-Sw250 test case, along with the turbulent periodic pipe.

Lastly, Table 2 summarizes the three test cases which are investigated in the present study, providing the values of the integral swirl number, $S_{\theta z}$, as computed from Equation (9). Furthermore, the computed ratios Δ/η, with $\Delta = \sqrt[3]{r\Delta_\theta \Delta_r \Delta_z}$ the characteristic mesh element size, and η the Kolmogorov's length scale, are lower than 3 all over the jet computational domain for any of the three test case configurations.

4 Effect of Vortex Breakdown Regimes on Evaporation

The effect of different swirling intensities and inflow profiles on the overall evaporation process is discussed here. Specifically, the inflow conditions investigated in the present work deliver peculiar VB states, which are of interest for what concerns flame
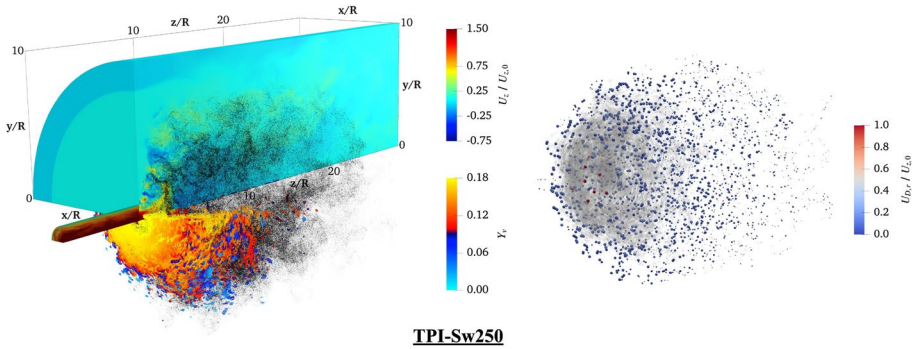
TPI-Sw250

Fig. 2 Turbulent-inflow case, TPI-Sw250. On the left: a sketch of a portion of the 3D cylindrical domain is illustrated; on the top, the colors contour the axial instantaneous velocity field within the jet, normalized by the bulk axial velocity, $U_{z,0}$; on the bottom, coherent vortex structures are visualized through Q-criterion isosurfaces, $Q = 0.1$, colored by the vapor mass fraction field; the whole droplet population is plotted with uniform-radius black points, i.e., droplets are not scaled by their size. On the right, in correspondence of the same time step: Q-criterion isosurfaces, $Q = 0.1$, are reported in grey; liquid droplets are scaled by their radius and colored by their radial velocity, $U_{D,r}$, normalized by $U_{z,0}$. Note that a different point of view was adopted to provide a clear insight into droplet spatial distribution, which could result in seeming inconsistency between the two figures

Table 2 Values of the integral swirl number, $S_{\theta z}$, calculated at $z/R = 0.25$ for the three test cases investigated in the present study

Test case	TPI-Sw250	MPI-S140	MPI-S200
$S_{\theta z}$	1.85	0.94	1.65

stabilization strategies adopted in stationary gas turbines and aero-engines. Therefore, the current study aims at providing an overview of how different VB regimes impact spray dynamics and evaporation, along with the spatial distribution of fuel vapor.

Different statistical quantities are provided. The statistical observables are computed over both the azimuthal direction, θ, i.e., the quantity of interest is integrated along the azimuthal direction, and time on the Eulerian grid. The Lagrangian mean quantities are computed by considering the entire droplet population - which amounts to almost 1.5M point droplets for each test case - and assigning the Lagrangian observable to be averaged to the related grid cell in the Eulerian framework. Furthermore, averages are computed after statistically-steady conditions have been attained, namely, each simulation is run for about $200R/U_{z,0}$ time scales before collecting the dataset, consistently with Dalla Barba and Picano (2018).

In the first place, Fig. 3 shows the contour plots of the mean axial, azimuthal, and radial velocities for the three test cases, normalized with respect to the bulk velocity, $U_{z,0}$, and overlapped with the mean velocity streamlines. For what concerns laminar-inflow configurations, a bubble-type VB characterizes the MPI-S140 case. In contrast, the high-swirl level imparted to the flow in the MPI-S200 case results in a regular conical VB, consistent with results of Moise and Mathew (2021). In both configurations, the vortex breakdown phenomenology leads to the onset of a stagnation point over the axis line and the establishment of a central recirculation region downstream. However, the location of the stagnation
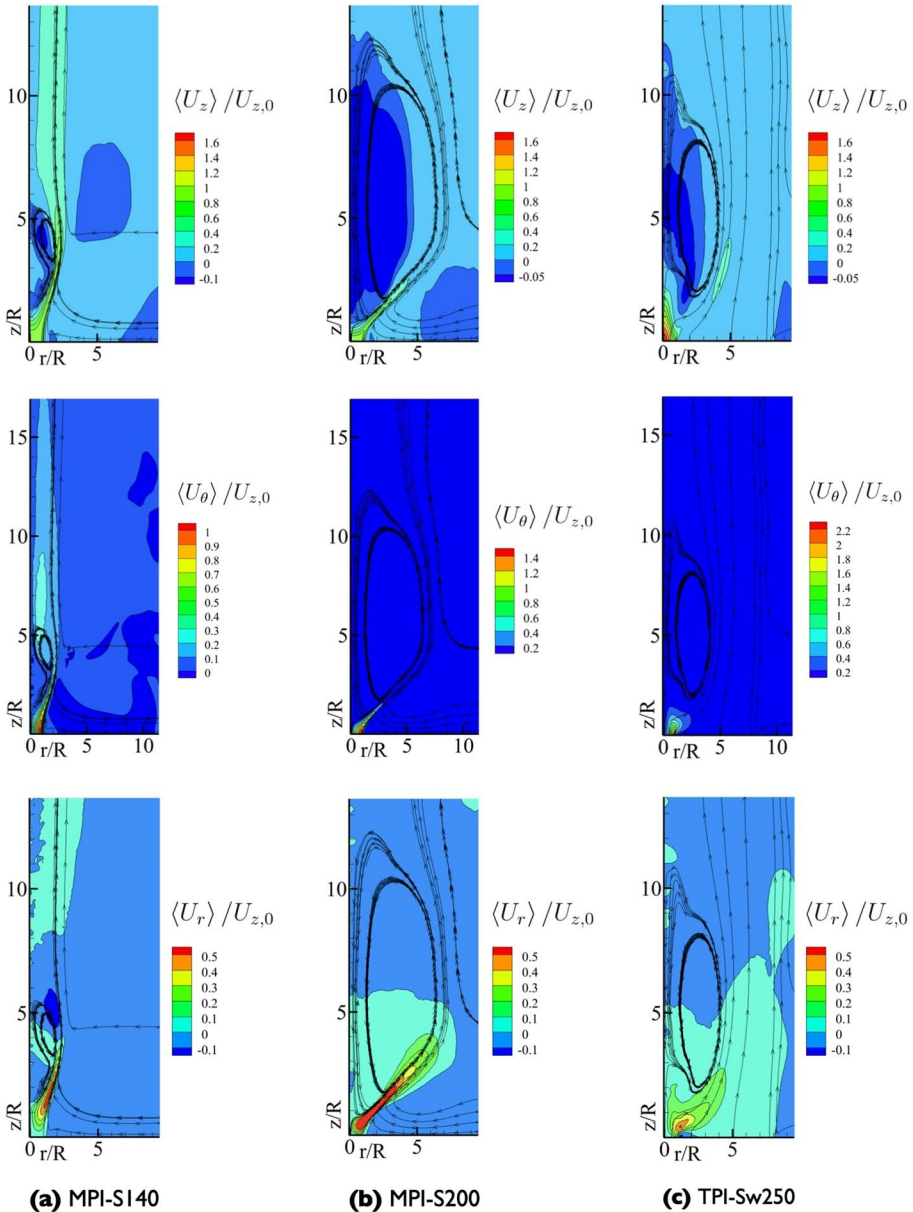
Fig. 3 Contour plots of the gas-phase mean velocity components, normalized with respect to the bulk velocity, $U_{z,0}$. The axial, azimuthal, and radial velocity components are provided from top to bottom. From left to right: **a** MPI-S140, **b** MPI-S200, **c** TPI-Sw250. Mean velocity streamlines are shown in black

point, the size of the reverse-flow zone, and the development of the flow pattern downstream of the VB-induced recirculation region strictly depend on the VB form. In fact, as the top line of Fig. 3a and b illustrates, the stagnation point moves closer to the injection orifice with increasing swirl intensity. Furthermore, for the MPI-S140 case, downstream of

the bubble structure, namely, beyond $z/R = 6$, there exists a recovery region, in which the vortex core appears to be expanded compared to the region upstream of the breakdown, and a defect in the axial velocity may be observed, as in typical wakes behind bluff bodies (Billant et al. 1998). In contrast, for the MPI-S200 case, the vortex expansion corresponding to the stagnation point is not followed by any contraction (Billant et al. 1998), and the enhanced jet spreading corresponds to a more prominent reverse flow zone. Furthermore, the decay of the azimuthal momentum is largely faster for the MPI-S200 case. The azimuthal component of the mean velocity flow field is almost depleted at $z/R = 1.5$, see the middle line of Fig. 3b. On the other hand, a peculiar jet topology can be observed in the TPI-Sw250 test case. While the swirling jet still undergoes VB, the VB-induced stagnation point appears to be downstream of the vortex expansion. In particular, a null value of the axial velocity on the centerline of the domain can be envisaged at $z/R \approx 3.5$, whereas a significant jet spreading due to VB phenomenology is already evident close to the injection orifice, i.e., upstream of $z/R = 1$, see the bottom line of Fig. 3c. Further downstream, the jet spreading progressively fades. In this regard, the corresponding shear layer wraps around a toroidal recirculation region, which shows a lesser extent in streamwise and radial directions than the MPI-S200 counterpart. Lastly, as evidenced by the middle line of Fig. 3c, the azimuthal momentum decays just downstream of the inflow section, namely, within the first radius into the cylindrical domain.

Figure 4 shows the contour lines of the mean liquid mass fraction, Φ_M, defined on the computational grid as $\Phi_M = m_l/m_g$, where m_l and m_g are the mean mass of liquid acetone and air inside each mesh cell, respectively. An accurate inspection of Fig. 4 reveals that the shape of the region where evaporation occurs strictly depends on the jet topology, as already evident from the close-up of the liquid droplets provided in Figs. 1 and 2. In the first place, under a bubble-type VB state, i.e., for the MPI-S140 test case, a significant presence of the liquid phase can also be found in the far field, namely, almost
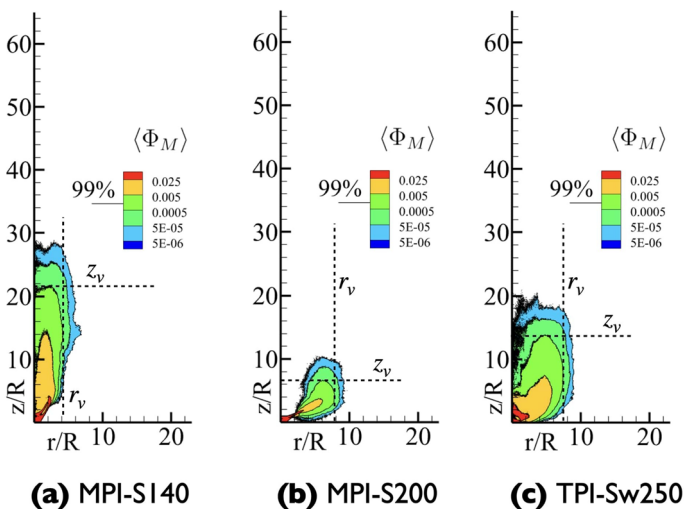

Fig. 4 Contour plots of the mean liquid mass fraction, $\Phi_M = m_l/m_g$, where m_l and m_g are the mean mass of liquid acetone and air inside each cell of the computational mesh, respectively. From left to right: **a** MPI-S140, **b** MPI-S200, **c** TPI-Sw250. The axial and radial spray vaporization lengths, z_v and r_v, are shown through dotted lines

up to $z/R = 30$, and the jet-axis region exhibits vaporization phenomena as well. Nonetheless, the medium-swirl level characterizing the MPI-S140 configuration results in moderate bending of the iso-contours of Φ_M close to the injection orifice, see Fig. 4a, as a result of restrained centrifugal forces acting on the carrier phase. Consequently, liquid acetone is not present beyond $r/R = 6$ in the radial direction. Concerning the MPI-S200 test case, the onset of a regular conical VB drastically affects the spatial distribution of the liquid phase and, thus, the locations where evaporation phenomena can be envisaged. In this regard, the high swirl intensity induced by the selected swirl rate, $S = 2.0$, produces high centrifugal forces in the swirling jet, which impact the radial advection of the liquid droplets just downstream of the inflow section. Therefore, the iso-contours of Φ_M are bent downwards, see Fig. 4b, and liquid acetone is exclusively present in the shear layer within the near field, i.e., up to $z/R = 2$. Furthermore, no point-droplets can be envisaged downstream of $z/R = 10$, while the region affected by evaporation extends up to $z/R = 10$ in the radial direction. On the other hand, the VB-induced central recirculation region is non-droplet-laden, depicting a completely different distribution of the vapor mass fraction, as further discussed in the following. Lastly, under the fully-turbulent pipe inflow conditions, i.e., for the TPI-Sw250 test case, prominent radial advection of liquid droplets is still evident in the near-field region, in that swirl intensity measured by $S_{\theta z}$ is comparable to that characterizing the MPI-S200 configuration. In fact, the droplet-laden region still extends up to $z/R = 10$ in the radial direction. Nevertheless, as already evidenced in Fig. 3c, turbulent-pipe inflow leads to a peculiar jet topology, with the stagnation point downstream of the vortex expansion induced by VB phenomenology. In this sense, this aspect is highlighted in Fig. 4c as well, in that liquid acetone droplets enter the VB-induced reverse flow zone, similar to what was observed under bubble-type VB conditions, and can be envisaged up to $z/R = 20$.

Based on results provided by Fig. 4, an overall axial vaporization length, z_v, is defined as the axial distance from the inflow section, where 99% of the injected liquid mass has transitioned to the vapor phase. In this respect, the minimum axial vaporization length results from the onset of a conical VB in the MPI-S200 test case, i.e., $z_v \approx 6.25$. On the other hand, the bubble-type VB established in the MPI-S140 test case does not induce any significant radial advection of the liquid droplets, with an axial vaporization length $z_v \approx 21.5$. Lastly, the turbulent-pipe-inflow configuration, i.e., TPI-Sw250, exhibits an axial vaporization length $z_v \approx 13.5$. These results are summarized in Fig. 5, which also reports the axial spray vaporization length exhibited by the swirling jets investigated in

Fig. 5 Axial spray vaporization length, z_v/R, as a function of the integral swirl number (Örlü and Alfredsson 2008), $S_{\theta z}$, and the bulk swirl number, Sw: effect of bubble vortex breakdown (BVB), conical vortex breakdown (CVB) and turbulent vortex breakdown (TVB). Red and blue points denote turbulent-pipe-inflow and laminar-inflow test cases investigated in the present work. In contrast, turbulent-pipe-inflow test cases investigated in Ciottoli et al. (2021) are denoted by green points
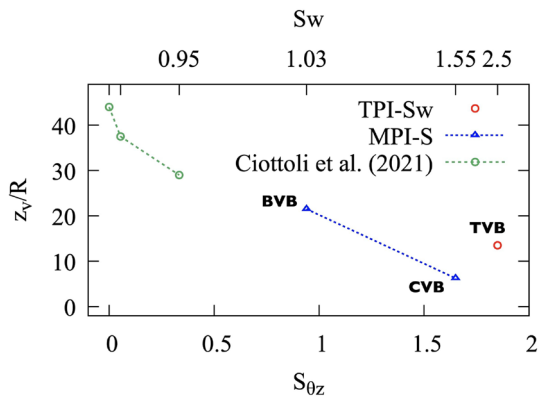
Ciottoli et al. (2021), where no breakdown was observed. As can be readily deduced, the onset of any VB state drastically affects the axial vaporization length.

Similarly, a radial vaporization length, r_v, is defined as the radial distance from the domain centerline, where 99% of the injected liquid mass has transitioned to the vapor phase. In this respect, the minimum radial vaporization length results from the onset of a bubble-type VB in the MPI-S140 test case, i.e., $r_v \approx 4$. In particular, as illustrated in Fig. 6, a bubble-type VB corresponds to a value of r_v comparable to those observed in the swirling jets investigated in Ciottoli et al. (2021), which were in turn characterized by restrained jet spreading due to the absence of VB. On the other hand, the significant swirl-induced centrifugal forces acting on the liquid phase in both MPI-S200 and TPI-Sw250 test cases translate into relevant radial advection of acetone droplets. Consequently, regular conical and turbulent VB states induce an increase in the radial vaporization length, i.e., $r_v \approx 7.5$.

A contour plot of the mean droplet radius, normalized by the droplet injection radius $r_{D,0} = 6 \ \mu m$, is reported in Fig. 7. The plot suggests that larger drops are radially advected in the proximity of the inflow due to the centrifugal forces associated with the swirl level, for any test case configuration. Nonetheless, completely different spatial distributions of liquid acetone droplets can be envisaged. Regarding the MPI-S140 test case, droplets are mostly concentrated in the core jet region, see Fig. 7a. Moreover, due to the axial velocity recovery region, droplets are axially advected downstream of the bubble structure and can be found up to $z/R \approx 30$. In contrast, concerning the MPI-S200 configuration, acetone droplets first follow the mixing layer evolution in the near field and are consequently advected towards the dry air environment, see Fig. 7b. Lastly, the TPI-Sw250 test case exhibits a significant presence of point droplets in the jet core region, particularly broad due to the onset of turbulent VB. Nonetheless, unlike the MPI-S140 configuration, liquid droplets experience a slight radial advection inside the central reverse flow zone.

The mean droplet vaporization rate and the vapor mass fraction distributions are displayed in Fig. 8 for the three inflow conditions. The plots of the former show how the vaporization is enhanced in the shear layer, attaining maximum values close to the inflow orifice, where large droplets enter in direct contact with the dry environmental air. Moreover, the spread angle and the topology of the evaporation region are consistent with the
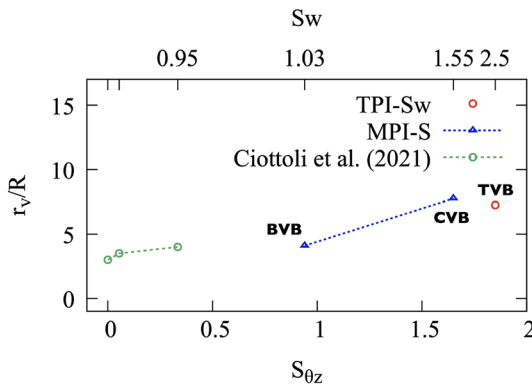

Fig. 6 Radial spray vaporization length, r_v/R, as a function of the integral swirl number (Örlü and Alfredsson 2008), $S_{\theta z}$, and the bulk swirl number, Sw: effect of bubble vortex breakdown (BVB), conical vortex breakdown (CVB) and turbulent vortex breakdown (TVB). Red and blue points denote turbulent-pipe-inflow and laminar-inflow test cases investigated in the present work. In contrast, turbulent-pipe-inflow test cases investigated in Ciottoli et al. (2021) are denoted by green points
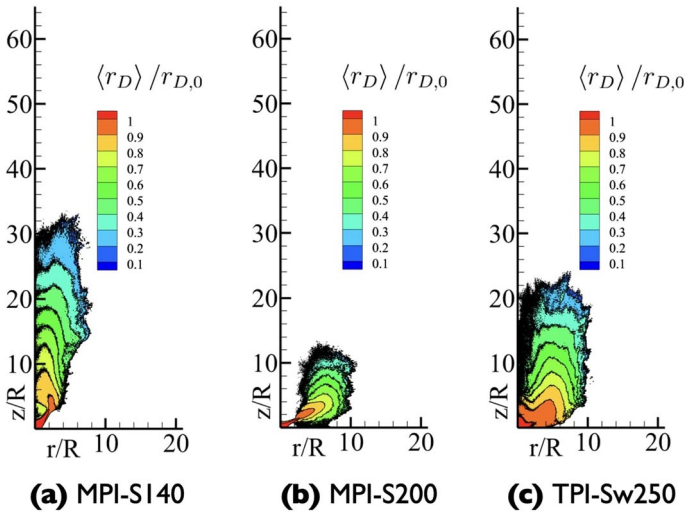
Fig. 7 Contour plots of the non-dimensional mean droplet radius. The reference length scale is the droplet injection radius, $r_{D,0} = 6\ \mu$m. From left to right: **a** MPI-S140, **b** MPI-S200, **c** TPI-Sw250

line of reasoning pursued when discussing the spatial distribution of the mean liquid mass fraction in Fig. 4. In particular, the MPI-S140 test case exhibits significant evaporation in the near-axis region up to $z/R \approx 20$, although to a lesser extent than what occurs in the proximity of the shear layer. This aspect has to be intended as a direct consequence of the entrainment phenomenon in the proximity of the outer portion of the shear layer. Indeed, in such a region, dry air meets the spray mixture, diminishing the vapor concentration and thus enhancing the overall vaporization. Conversely, the inner jet core is prevented from reaching the outer region. It is also affected by the VB-induced reverse flow phenomenon, thus exhibiting higher saturation levels, as evidenced by the spatial distribution of the vapor mass fraction in Fig. 8a. Similar considerations apply to the TPI-Sw250 test case, which shows a significant vapor mass fraction along the centerline of the domain. However, less relevant evaporation is observed around the jet-axis region, see Fig. 8c, as a result of the different spatial distribution of liquid droplets evidenced by Fig. 7c. Lastly, under the conical VB conditions which characterize the MPI-S200 configuration, the maximum evaporation rate can be envisaged in both the inner and outer portions of the shear layer near the inflow section. Further downstream, the residual azimuthal momentum of the swirling jet still contributes to the radial advection of liquid droplets towards the dry-air environment, enhancing the overall vaporization. In contrast, due to the lack of droplets in the jet core region, no evaporation can be envisaged in the VB-induced central recirculation zone, which is characterized by almost vanishing saturation levels, as evident from the spatial distribution of the vapor mass fraction in Fig. 8b.

The axial distribution of the non-dimensional mean axial velocity is provided in Fig. 9a. The plot shows the strong influence of the inflow conditions on the centerline velocity decay. In this regard, it is again evident how the MPI-S200 test case shows the largest central recirculation region due to the regular conical VB state. In contrast, the axial velocity recovery region becomes evident for the MPI-S140 configuration beyond $z/R = 5$. Under the conical VB state, no liquid droplets can be detected on the centerline downstream of the stagnation point, as shown by Fig. 9b. In contrast, liquid droplets enter the reverse flow
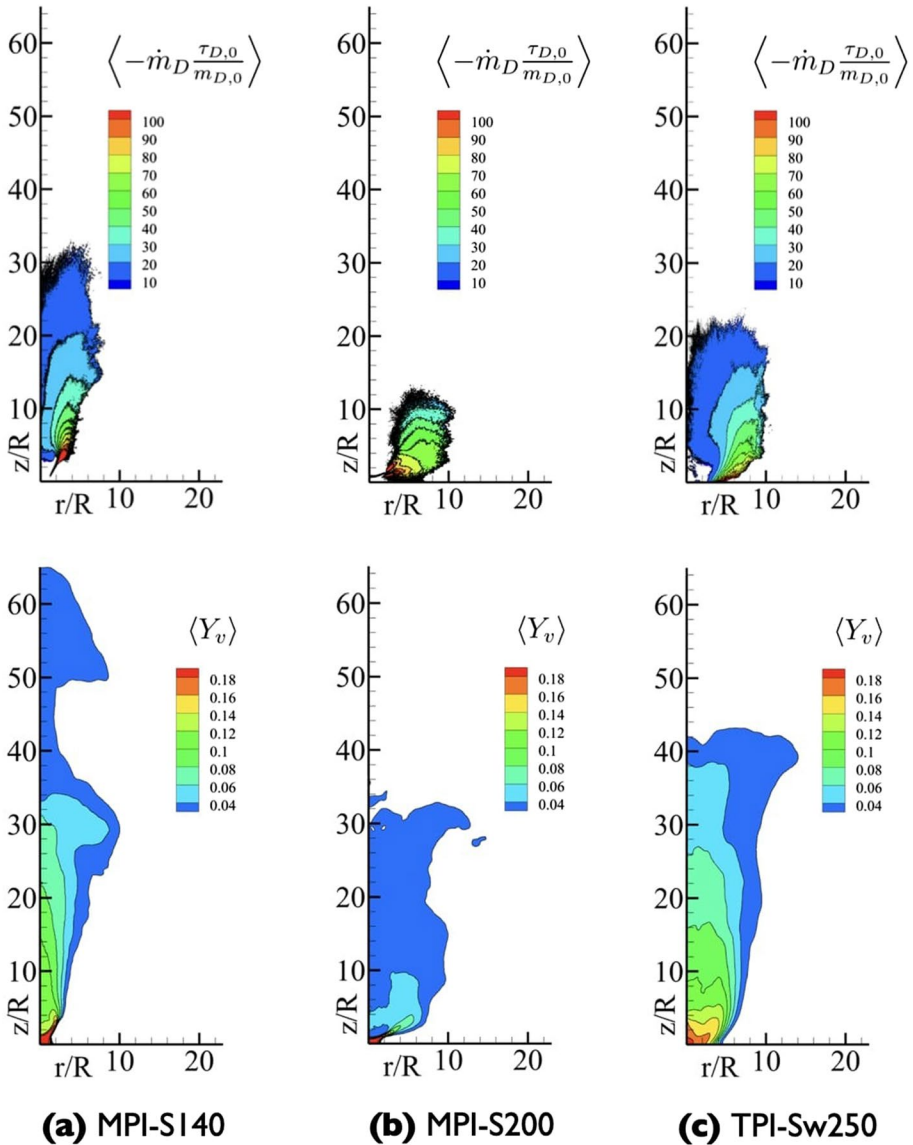
Fig. 8 Contour plots of the non-dimensional mean droplet vaporization rate (top) and mean vapor mass fraction (bottom). The reference scale is defined as $\dot{m}_{D,0} = m_{D,0}/\tau_{D,0}$, with $m_{D,0}$ the initial droplet mass and $\tau_{D,0}$ the initial droplet relaxation time. From left to right: **a** MPI-S140, **b** MPI-S200, **c** TPI-Sw250

zone under fully-turbulent pipe inflow conditions. Still, they are then radially advected by the mean flow, so that almost no liquid phase can be detected on the jet axis beyond $z/R = 10$. Concerning the MPI-S140 test case, while larger drops are advected by the centrifugal forces upstream of the stagnation point, i.e., upstream of $z/R = 1$, a relevant presence of smaller droplets can be traced on the centerline up to $z/R = 30$. In this regard, the overall vaporization process of the liquid phase in the near-axis zone for the MPI-S140
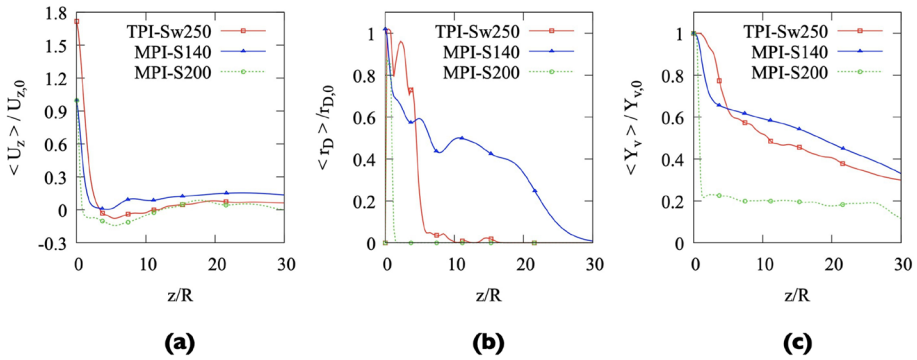
Fig. 9 Axial distributions of **a** gas-phase mean axial velocity, **b** mean droplet radius, and **c** mean vapor mass fraction computed on the centerline of the domain. Each quantity is non-dimensional, the reference scales being set to the bulk inflow velocity, $U_{z,0}$, and the initial droplet radius, $r_{D,0}$

configuration is slowed down by the significant saturation levels experienced by the flow in such a region, as can be deduced by the spatial distribution of vapor mass fraction, Y_v shown in Fig. 9c. In particular, the trend encountered in the evolution of Y_v downstream of the stagnation point closely resembles that characterizing the TPI-Sw250 test case. Thus, although the spray gets broader under turbulent inflow conditions, the evolution of the vapor mass fraction inside the jet core region is similar to the MPI-S140 test case, as already evidenced in Fig. 8. Conversely, regarding the MPI-S200 test cases, no liquid droplets enter the VB-induced recirculation region, which is thus characterized by extremely low saturation levels, see Fig. 9c.

Finally, the sensitivity of the droplet dimension to the inflow conditions is investigated through the probability density function (PDF) of the droplet radius evaluated at different axial distances from the origin, normalized by the corresponding vaporization length, as reported in Fig. 10. Since the inflow condition is a monodisperse suspension, in all the test cases, the PDF at the inflow section is a Dirac delta function centered at $r_D/r_{D,0} = 1$. For the MPI-S200 test case, the PDF of the droplet radius is still a Dirac delta function up to 10% of the spray vaporization length, where the VB-associated stagnation point is found. Downstream of such axial location, the entire liquid droplets are radially advected towards dry environmental air and undergo evaporation. This is confirmed by the evolution of the PDF beyond $z/z_v = 0.25$, with a polydisperse suspension observed at $z/z_v = 0.5$. On the other hand, as a consequence of the completely different jet topology originating from a bubble-type VB, for the MPI-S140 test case, a significant spread in the statistical
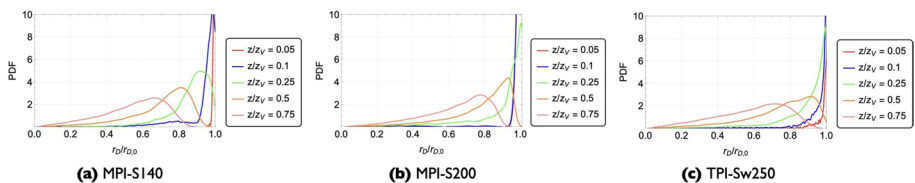

Fig. 10 Probability density function of the non-dimensional droplet radius at different axial distances from the inflow section, normalized by the spray vaporization length, z_v. From left to right: **a** MPI-S140, **b** MPI-S200, **c** TPI-Sw250

distribution of droplet radius is already observed at 25% of the spray vaporization length, i.e., in the proximity of the final section of the bubble structure. Lastly, regarding the TPI-Sw250 configuration, the PDF of the droplet radius spans a restricted range up to $z/z_v = 0.25$, which nearly coincides with the axial location of the stagnation point, downstream of which larger drops are radially advected through the mixing layer and lead to a polydisperse suspension.

The previous observations confirm how the different swirl levels and velocity inflow conditions impact the jet topology, thus affecting the spatial distribution of liquid droplets and vapor mass fraction. In this sense, in the conditions of the test cases taken into consideration, the ambient temperature and pressure are kept constant, and the droplets are injected into a nearly saturated flow. Hence, a non-zero evaporation rate can only result from a decreased vapor mass fraction surrounding each liquid drop, which may derive from either the radial advection of the dispersed phase towards dry environmental air or the mixing between the carrier mixture and the surrounding dry air. In particular, based on the results provided above, it is clear how the establishment of various vortex breakdown states induces different dispersion mechanisms acting on the dispersed phase, thus drastically affecting the overall evaporation process and the spray vaporization length.

5 Effect of Droplet Inertia on Evaporation

The interaction of finite droplet inertia with the carrier phase turbulent dynamics is well-known as a driving process for the small-scale clustering of droplets (Gualtieri et al. 2012), thus affecting the overall vaporization process (Dalla Barba and Picano 2018). In this regard, the effectiveness of the inertial effects on the evaporation of the liquid droplets is inquired through an additional set of three simulations, whose setup is identical to the previous ones, except for the lack of inertial effects on the dispersed phase. The point-droplets are thus treated as Lagrangian tracers.

Under this assumption, the trajectory of each point-droplet is constrained to the carrier phase velocity field, i.e., $\boldsymbol{u}_D = \boldsymbol{u}|_{\boldsymbol{x}=\boldsymbol{x}_D}$, while the right-hand side term in Eq. 7 is imposed to zero. In this new set of simulations, hereinafter referred to as *tracer simulations*, droplets experience a vanishing aerodynamic response time, and thus their motion is bound to the local motion of the carrier mixture.

A comparison between the mean distribution of the droplet non-dimensional radius in the baseline simulations with those obtained in the tracer simulations is reported in Fig. 11 for the three test case configurations. Again, radial distributions at different axial locations, normalized by the corresponding spray vaporization length, are investigated. Under fully-turbulent pipe inflow conditions, i.e., for the TPI-Sw250 configuration, the role of the droplet inertial effects on the evaporation is almost negligible in the near field, as can be deduced from the radial distribution of the droplet non-dimensional radius at $z/z_v = 0.25$. Further downstream, at 50% of the spray vaporization length, inertial effects play a minor role in the interaction between the mixing layer and the dry-air environment, namely, beyond $r/R = 5$. Indeed, when inertial effects are included, the droplet radii decrease slightly faster than the tracer solutions. A similar trend can be envisaged at $z/z_v = 0.75$, where minor differences are also encountered within the jet core region. Therefore, it can be concluded that droplet inertial effects impact the overall evaporation process to a small extent under turbulent inflow conditions as a consequence of intense turbulent mixing already well-established close to the injection orifice. Similarly, concerning the MPI-S200
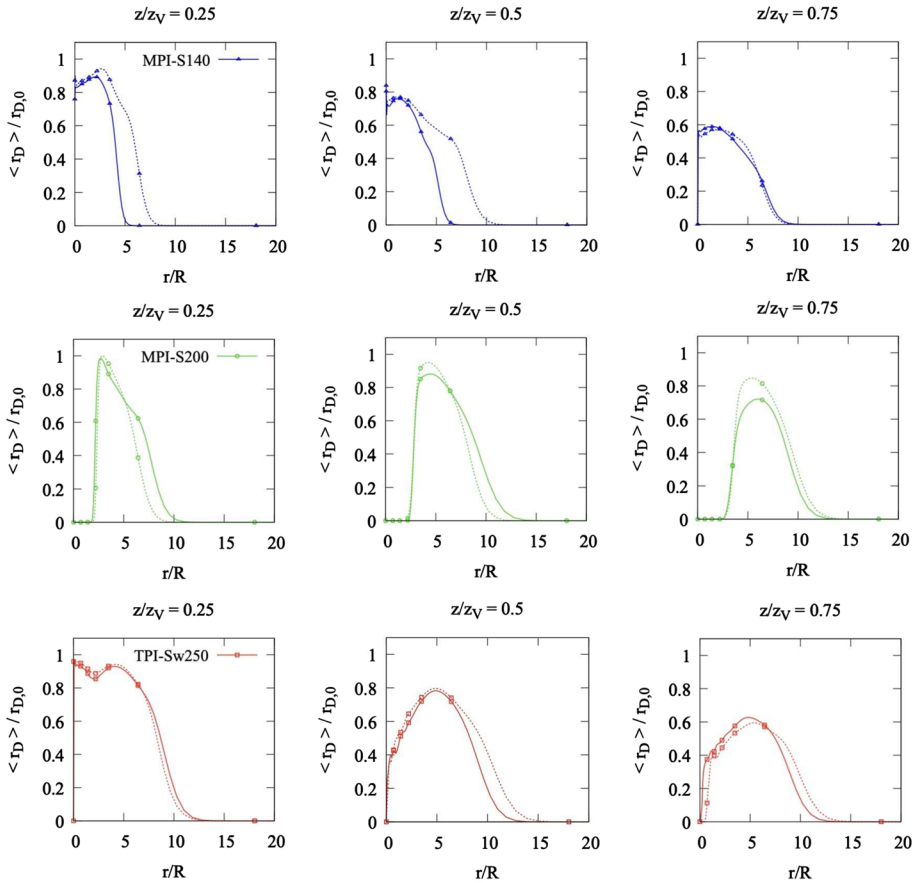
Fig. 11 Mean distribution of the non-dimensional droplet radius, $\langle r_D \rangle / r_{D,0}$, as a function of the radial distance from the jet axis. The plots provide the baseline results (solid lines) and those obtained under the Lagrangian tracer approximation (dotted lines). The plots for the three test cases at different axial distances are provided from top to bottom, normalized by the spray vaporization length

configuration, droplet inertial effects play a secondary role. Indeed, up to 50% of the spray vaporization length, minor differences in the evaporation process can only be detected in the vicinity of the mixing layer, where the droplet radii decrease slightly slower in the presence of inertial effects. In this situation, the restrained influence of inertial effects on phase transition can be ascribed to the extremely high centrifugal forces experienced by the swirling jet due to the onset of a conical VB. In particular, the latter play a prominent role in droplet dispersion and evaporation, regardless of the aerodynamic response properties of the dispersed phase. In contrast, the effects of droplet inertia on the evaporation process are more evident for the MPI-S140 test case. In particular, up to 50% of the spray vaporization length, inertial effects contribute to enhanced evaporation of liquid droplets in the proximity of the mixing layer, i.e., beyond $r/R = 3$. Conversely, in the spray far field, at $z/z_v = 0.75$, the droplet radius distributions almost coincide in the tracer and the baseline simulations. This aspect is consistent with the progressive decrease of the droplets' mass and an increase of the turbulent time scales in the downstream evolution of the flow,

resulting in a substantial diminution of the droplet response time in the far field (Dalla Barba and Picano 2018).

To rigorously quantify the effects of the swirled inflows on the droplet dynamics, a *swirl Stokes* number is introduced as:

$$St_{sw} = \frac{\tau_D}{\tau_{sw}} = \frac{d_D^2}{18\nu} \frac{\rho_l}{\rho} \frac{U_\theta}{x_{D,r}}, \tag{12}$$

where $\tau_D = d_D^2/(18\nu)(\rho_l/\rho)$ indicates the droplet relaxation time, whereas $\tau_{sw} = x_{D,r}/U_\theta$ is a rotational velocity time scale, being U_θ the azimuthal velocity of the carrier phase at the droplet location and $x_{D,r}$ the radial position of the droplet with respect to the jet axis. The mean values of the swirl-based Stokes number and the non-dimensional droplet radius distributions are reported in Fig. 12. The maximum values of the swirl-based Stokes number are located where both the mean angular velocity and the mean droplet radius peak, i.e., close to the injector pipe walls, where $x_{D,r} = R$, and the droplet diameter is maximum, namely, $d_D = d_{D,max}$, for the three test case configurations. In those regions, the effect of centrifugal forces on the droplets is expected to result in an acceleration in the radial direction, with the effect of observing droplets with a radial velocity higher than the one of the carrier phase, thus with an enhancement in the radial advection of liquid drops.

Regardless of the inflow conditions, from Fig. 12, it is evident how significant effects on droplet dynamics induced by the swirling motion exclusively extend up to the first portion of the velocity shear layer, namely, in the proximity of the vortex expansion associated with the VB phenomenology. In fact, such a region is characterized by the highest values of the azimuthal velocity in the carrier phase and the largest liquid drops. In contrast, in the downstream evolution of the jet flow, due to the fast decay of azimuthal momentum for any test case configuration, the evaporation process is barely affected by swirl-induced centrifugal forces.
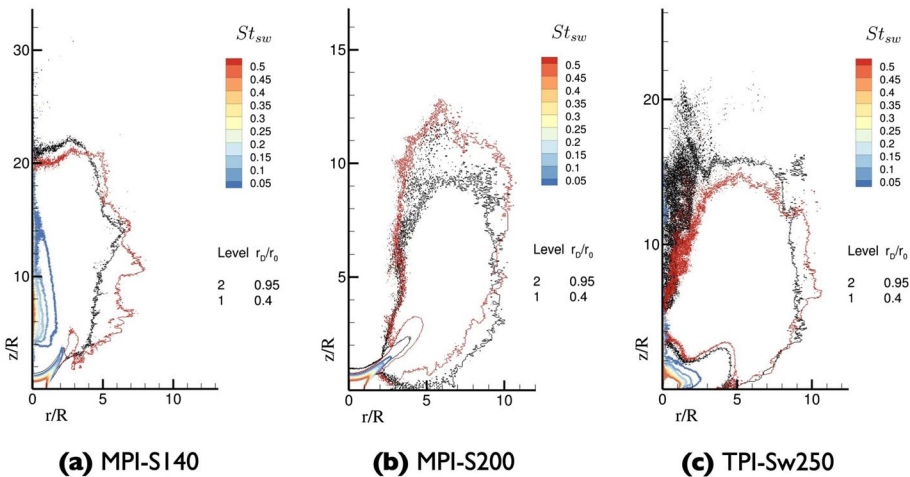

(a) MPI-S140   **(b)** MPI-S200   **(c)** TPI-Sw250

Fig. 12 Iso-lines of the mean distribution of the non-dimensional droplet radius, $\langle r_D \rangle / r_{D,0}$, and contour plots of the swirl-based Stokes number. Two levels of the non-dimensional droplet radius are considered, i.e., $\langle r_D \rangle / r_{D,0} = 0.4$ and $\langle r_D \rangle / r_{D,0} = 0.95$. The baseline solution is in black, while the Lagrangian tracer solution is in red. From left to right: **a** MPI-S140, **b** MPI-S200, **c** TPI-Sw250

6 Conclusions

The effects of different vortex breakdown states on swirling jets laden with acetone droplets are investigated by means of direct numerical simulations. The numerical method is based on the low-Mach number expansion of the Navier–Stokes equations for the Eulerian carrier phase, coupled with a Lagrangian description of the dispersed phase based on the point-droplet model. This approach allows taking into account for density variations in the carrier phase as well as for a two-way coupling between the phases. The present numerical study focuses on the dilute regime of the overall downstream evolution of jet sprays, where the major part of the liquid phase evaporates. The study provides the outcomes of different DNSs reproducing an air-acetone mixture laden with liquid acetone droplets injected into an open environment in nearly-saturated conditions. Three cases with different velocity inflow conditions are considered: (i) TPI-Sw250, where fully-turbulent pipe inflow conditions result in a turbulent vortex breakdown; (ii) MPI-S140, where the inflow conditions are imposed according to a laminar Maxworthy velocity profile with swirl rate $S = 1.4$, leading to the onset of a bubble-type vortex breakdown; (iii) MPI-S200, where the inflow conditions are imposed according to a laminar Maxworthy velocity profile with swirl rate $S = 1.4$, leading to the onset of a regular conical vortex breakdown. It is found that a conical vortex breakdown leads to an enhancement of the overall evaporation rate of the dispersed phase, with a substantially lower spray penetration length than the TPI-Sw250 and MPI-S140 test cases. This effect is found to be related to the extremely high centrifugal forces experienced by the swirling jet under the MPI-S200 inflow conditions. In particular, in the presence of a conical vortex breakdown, in the proximity of the injection orifice, the entire liquid droplets are radially advected towards the low-saturation mixing layer of the jet, thus increasing their evaporation rate. In contrast, for both the TPI-Sw250 and the MPI-S140 configurations, a significant portion of liquid drops show considerable aerodynamic response properties to overcome the carrier-phase centrifugal forces near the inflow section, thus entering the central recirculation region induced by the vortex breakdown. Consequently, the reverse flow zone exhibits substantially higher saturation levels compared with the conical vortex breakdown counterpart, thus slowing down the overall evaporation process.

The influence of the swirling intensity and the related centrifugal forces on the motion and evaporation of the droplets is further inquired by employing an additional set of DNSs in which the droplet dynamics is reduced to that of passive Lagrangian tracers. Again, the jet topologies resulting from different vortex breakdown states affect the role of inertial effects: (i) for the TPI-Sw250 test case, droplet inertial effects impact the overall evaporation process to a small extent, as a consequence of intense turbulent mixing already well-established close to the injection orifice; (ii) for the MPI-S140, inertial effects are more evident, and contribute to enhanced evaporation of liquid droplets in the proximity of the mixing layer up to 50% of the vaporization length; (iii) for the MPI-S200, droplet inertial effects play a secondary role, in that the extremely high centrifugal forces experienced by the swirling jet drive droplet dispersion and evaporation processes, regardless of the aerodynamic response properties of the dispersed phase. Inertial effects have also been quantified by means of a purposely defined swirl Stokes number. In particular, the maximum values of the swirl-based Stokes number are attained up to the first portion of the velocity shear layer for any test case configuration, whereas the evaporation process is barely affected in the downstream evolution of the jet flow due to the fast decay of azimuthal momentum characterizing the swirling jets being investigated.

Declarations

Conflict of interest The authors declare that they have no conflict of interest.

Ethical approval Not applicable.

Informed consent Not applicable.

References

Apte, S., Moin, P.: Spray modeling and predictive simulations in realistic gas-turbine engines. In: Ashgriz, N. (ed.) Handbook of Atomization and Sprays, pp. 811–835. Springer, Boston (2011)

Arienti, M., Li, X., Soteriou, M., et al.: Coupled level-set/volume-of-fluid method for simulation of injector atomization. J. Propuls. Power. **29**(1), 147–157 (2013)

Balachandar, S., Eaton, J.: Turbulent dispersed multiphase flow. Annu. Rev. Fluid. Mech. **42**, 111–133 (2010)

Battista, F., Picano, F.: Casciola C turbulent mixing of a slightly supercritical van der Waals fluid at low-Mach number. Phys. Fluids **26**(5), 55–101 (2014)

Battista, F., Troiani, G., Picano, F.: Fractal scaling of turbulent premixed flame fronts: application to LES. Int. J. Heat Fluid Flow **51**, 78–87 (2015)

Billant, P., Chomaz, J., Huerre, P.: Experimental study of vortex breakdown in swirling jets. J. Fluid Mech **376**, 183–219 (1998)

Bukhvostova, A., Russo, E., Kuerten, J., et al.: Comparison of DNS of compressible and incompressible turbulent droplet-laden heated channel flow with phase transition. Int. J. Multiph. Flow **63**, 68–81 (2014)

Casciola, C., Gualtieri, P., Picano, F., et al.: Dynamics of inertial particles in free jets. Phys. Scr. **2010**(142), 14 (2010)

Cavalieri, D., Liberatori, J., Malpica Galassi, R., et al.: Unsteady RANS Simulations with Uncertainty Quantification of Spray Combustor Under Liquid Rocket Engine Relevant Conditions. (2023). https://doi.org/10.2514/6.2023-2148 AIAA SciTech 2023 Forum, National Harbor, MD & Online, 23-27 January 2023

Chen, Y.C., Stårner, S., Masri, A.: A detailed experimental investigation of well-defined, turbulent evaporating spray jets of acetone. Int. J. Multiph. Flow **32**(4), 389–412 (2006)

Ciottoli, P., Lee, B., Lapenna, P., et al.: Large eddy simulation on the effects of pressure on syngas/air turbulent nonpremixed jet flames. Combust. Sci. Technol. **192**(10), 1963–1996 (2020)

Ciottoli, P., Battista, F., Malpica Galassi, R., et al.: Direct numerical simulations of the evaporation of dilute sprays in turbulent swirling jets. Flow Turbul. Combust. **106**, 993–1015 (2021)

Ciottoli P, Petrocchi A, Angelilli L, et al Uncertainty Quantification Analysis of RANS of Spray Jets. AIAA Propulsion and Energy 2020 Forum, Virtual Event, 24–28 August 2020 (2020b) https://doi.org/10.2514/6.2020-3882

Dalla Barba, F., Picano, F.: Clustering and entrainment effects on the evaporation of dilute droplets in a turbulent jet. Phys. Rev. Fluids **3**(034), 304 (2018)

Druzhinin, O., Elghobashi, S.: Direct numerical simulations of bubble-laden turbulent flows using the two-fluid formulation. Phys. Fluids **10**(3), 685–697 (1998)

Eckel, G., Grohmann, J., Cantu, L., et al.: LES of a swirl-stabilized kerosene spray flame with a multi-component vaporization model and detailed chemistry. Combust. Flame **207**, 134–152 (2019)

Elghobashi, S.: Particle-laden turbulent flows: direct simulation and closure models. Appl. Sci. Res. **48**, 301–314 (1991)

Facciolo, L., Tillmark, N., Talamelli, A., et al.: A study of swirling turbulent pipe and jet flows. Phys. Fluids **19**(3), 35–105 (2007)

Faeth, G., Hsiang, L.P., Wu, P.K.: Structure and breakup properties of sprays. Int. J. Multiph. Flow **21**, 99–127 (1995)

Giusti, A., Kotzagianni, M., Mastorakos, E.: LES/CMC simulations of swirl-stabilised ethanol spray flames approaching blow-off. Flow Turbul. Combust. **97**, 1165–1184 (2016)

Gualtieri, P., Picano, F., Sardina, G., et al.: Statistics of particle pair relative velocity in the homogeneous shear flow. Phys. D Nonlinear Phenom. **241**(3), 245–250 (2012)

Gui, N., Fan, J., Chen, S.: The effects of flow structure and particle mass loading on particle dispersion in particle-laden swirling jets. Phys. Lett. A **375**(4), 844–893 (2011)

Jones, W., Marquis, A., Vogiatzaki, K.: Large-eddy simulation of spray combustion in a gas turbine combustor. Combust. Flame **161**(1), 222–239 (2014)

Li, Y., Rybdylova, O.: Application of the generalised fully Lagrangian approach to simulating polydisperse gas-droplet flows. Int. J. Multiph. Flow **142**(103), 716 (2021)

Liberatori, J., Malpica Galassi, R., Liuzzi, D., et al. Uncertainty quantification in RANS prediction of LOX cross-flow injection in Methane. In: AIAA Propulsion and Energy 2021 Forum, Virtual Event, 9–11 August 2021 (2021). https://doi.org/10.2514/6.2021-3570

Liberatori, J., Malpica Galassi, R., Valorani, M., et al.: Uncertainty quantification analysis of Reynolds-averaged Navier-Stokes simulation of spray swirling jets undergoing vortex breakdown. Int. J. Spray Combust. Dyn. (2023). https://doi.org/10.1177/17568277231183047

Lilley, D.: Swirl flows in combustion: a review. AIAA J. **15**(8), 1063–1078 (1977)

Lucca-Negro, O., O'Doherty, T.: Vortex breakdown: a review. Prog. Energy Combust. Sci. **27**(4), 431–481 (2001)

Luo, K., Pitsch, H., Pai, M., et al.: Direct numerical simulations and analysis of three-dimensional n-heptane spray flames in a model swirl combustor. Proc. Combust. Inst. **33**(2), 2143–2152 (2011)

MacKay, D.: Information Theory, Inference, and Learning Algorithms. Cambridge University Press, Cambridge (2005)

Majda, A., Sethian, J.: The Derivation and Numerical Solution of the Equations for Zero Mach Number Combustion. Combust. Sci. Technol. **42**(3–4), 185–205 (1985)

Mashayek, F.: Direct numerical simulations of evaporating droplet dispersion in forced low Mach number turbulence. Int. J. Heat Mass Transf. **41**(17), 2601–2617 (1998)

Meier, U., Heinze, J., Freitag, S., et al.: Spray and flame structure of a generic injector at aeroengine conditions. J. Eng. Gas Turbines Power **134**(3), 31–503 (2012)

Menon, S., Ranjan, R.: Spray combustion in swirling flow. In: Grinstein, F. (ed.) Coarse Grained Simulation and Turbulent Mixing, pp. 351–392. Cambridge University Press, Cambridge (2016)

Miller, R., Bellan, J.: Direct numerical simulation of a confined three-dimensional gas mixing layer with one evaporating hydrocarbon-droplet-laden stream. J. Fluid Mech. **384**, 293–338 (1999)

Moise, P., Mathew, J.: Hysteresis and turbulent vortex breakdown in transitional swirling jets. J. Fluid Mech. **915**, A94 (2021)

Örlü, R., Alfredsson, P.: An experimental study of the near-field mixing characteristics of a swirling jet. Flow Turbul. Combust. **80**, 323–350 (2008)

Osiptsov, A.: Lagrangian modelling of dust admixture in gas flows. Astrophys. Space Sci. **274**(1–2), 377–386 (2000)

Pai, G., Subramaniam, S.: Accurate numerical solution of the spray equation using particle methods. At. Sprays **16**(2), 159–194 (2006)

Patel, N., Menon, S.: Simulation of spray-turbulence-flame interactions in a lean direct injection combustor. Combust. Flame **153**(1–2), 228–257 (2008)

Puggelli, S., Bertini, D., Mazzei, L., et al.: Scale adaptive simulations of a swirl stabilized spray flame using flamelet generated manifold. Energy Procedia. **101**, 1143–1150 (2016)

Rocco, G., Battista, F., Picano, F., et al.: Curvature Effects in Turbulent Premixed Flames of H2/Air: a DNS Study with Reduced Chemistry. Flow Turbul. Combust. **94**, 359–379 (2015)

Ruith, M., Chen, P., Meiburg, E.: Development of boundary conditions for direct numerical simulations of three-dimensional vortex breakdown phenomena in semi-infinite domains. Comput. Fluids **33**(9), 1225–1250 (2004)

Sankaran, V., Menon, S.: LES of spray combustion in swirling flows. J. Turbul. **3**, 011 (2002)

Senoner, J., Sanjosé, M., Lederlin, T., et al.: Eulerian and Lagrangian Large-Eddy Simulations of an evaporating two-phase flow. C R Mec. **337**(6–7), 458–468 (2009)

Shen, Y., Ghulam, M., Zhang, K., et al.: Vortex breakdown of the swirling flow in a lean direct injection burner. Phys. Fluids **32**(125), 118 (2020)

Subramaniam, S.: Lagrangian-Eulerian methods for multiphase flows. Prog. Energy Combust. Sci. **39**(2–3), 215–245 (2013)

Syred, N., Beér, J.: Combustion in swirling flows: A review. Combust. Flame **23**(2), 143–201 (1974)

Villermaux, E., Moutte, A., Amielh, M., et al.: Fine structure of the vapor field in evaporating dense sprays. Phys. Rev. Fluids **2**(074), 501 (2017)

Waterson, N., Deconinck, H.: Design principles for bounded higher-order convection schemes - a unified approach. J. Comput. Phys. **224**(1), 182–207 (2007)

Williams, F.: Spray combustion and atomization. Phys. Fluids **1**, 541–545 (1958)

Wu, Y., Carlsson, C., Szasz, R., et al.: Effect of geometrical contraction on vortex breakdown of swirling turbulent flow in a model combustor. Fuel **170**, 210–225 (2016)

Authors and Affiliations

Jacopo Liberatori[1] · Francesco Battista[1] · Federico Dalla Barba[2] · Pietro Paolo Ciottoli[1]

✉ Jacopo Liberatori
  jacopo.liberatori@uniroma1.it

  Francesco Battista
  francesco.battista@uniroma1.it

  Federico Dalla Barba
  federico.dallabarba@unipd.it

  Pietro Paolo Ciottoli
  pietropaolo.ciottoli@uniroma1.it

[1] Department of Mechanical and Aerospace Engineering, Sapienza University of Rome, Via Eudossiana 18, 00184 Rome, Italy

[2] Department of Industrial Engineering & CISAS, University of Padova, Via Venezia 1, 35131 Padua, Italy